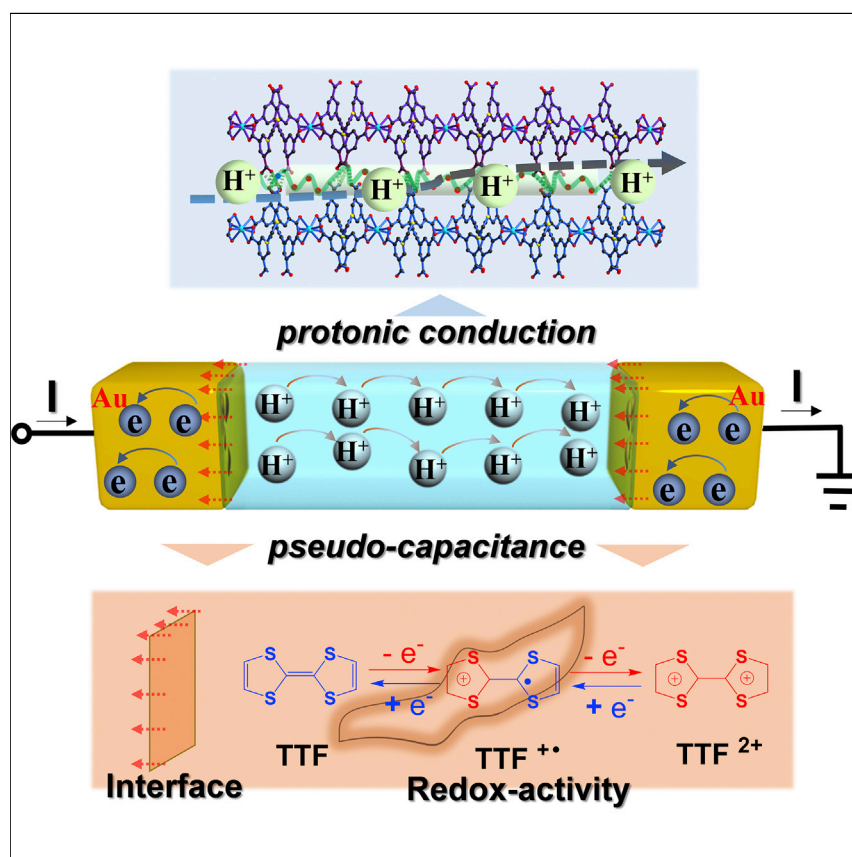


Article

High Electrical Conductivity in a 2D MOF with Intrinsic Superprotonic Conduction and Interfacial Pseudo-capacitance



Jian Su, Wen He, Xiao-Min Li, ...,
Ya-Qian Lan, Mengning Ding,
Jing-Lin Zuo

yqlan@njun.edu.cn (Y.-Q.L.)
mding@nju.edu.cn (M.D.)
zuojl@nju.edu.cn (J.-L.Z.)

HIGHLIGHTS

Topology-guided design strategy
for 2D MOFs

High proton conductivity in a 2D
MOF with spatially installed
carboxyl groups

High electrical conductivity
enabled by protonic/pseudo-
capacitance coupling mechanism

Integrating efficient ionic and electrical conduction in metal-organic frameworks (MOFs) is desired for their applications in clean energy technologies. We present the rational design and synthesis of an MOF with unbound carboxyl groups that facilitate high proton conductivity and redox-active ligands that mediate efficient electrical conduction at the MOF-metal interface through a coupled ionic/pseudo-capacitive conduction mechanism. The design strategy presented here offers guidance to the future development of ionically and electrically conductive MOFs for energy-storage devices.



Demonstrate

Proof-of-concept of performance with
intended application/response

Su et al., Matter 2, 711–722
March 4, 2020 © 2019 Elsevier Inc.
<https://doi.org/10.1016/j.matt.2019.12.018>



Article

High Electrical Conductivity in a 2D MOF with Intrinsic Superprotonic Conduction and Interfacial Pseudo-capacitance

Jian Su,^{1,5} Wen He,^{2,5} Xiao-Min Li,^{3,5} Lei Sun,⁴ Hai-Ying Wang,¹ Ya-Qian Lan,^{3,*} Mengning Ding,^{2,*} and Jing-Lin Zuo^{1,6,*}

SUMMARY

Two-dimensional (2D) conductive metal-organic frameworks (MOFs), whose advanced electrical properties accompany their intrinsic structural characteristics, represent an exciting new class of 2D atomic crystals for the van der Waals integration of novel heterostructures and the development of novel nano/quantum devices. Guided by topology, we report two 2D MOFs (1 and 2) constructed via combination of $[\text{In}(\text{COO})_4]^-$ metal nodes and tetratopic tetrathiafulvalene (TTF)-based linkers, with ultrahigh proton conductivity (6.66×10^{-4} and $1.30 \times 10^{-2} \text{ S cm}^{-1}$ for 1 and 2, respectively). Additionally, high electrical conductivity was simultaneously achieved with the pure protonic nature of the 2D MOF 2. The electrical conduction at the MOF-metal interface is enabled by the redox-switchable behavior of the TTF-based ligands. This unique charge-transport mechanism, protonic/pseudo-capacitance coupling, offers a new strategy for utilizing the ionic conductivity from MOFs to construct functional electronic devices.

INTRODUCTION

The unique optical and electrical properties of graphene, transition-metal dichalcogenides, black phosphorus, and other inorganic two-dimensional (2D) materials have boosted research interest in layered materials.^{1–3} As a result, 2D atomic crystals have been widely applied in a variety of fields including energy, environment, and healthcare.^{4–7} In contrast to inorganic 2D materials, 2D metal-organic frameworks (MOFs) can be formed through self-assembly of designable organic linkers and selected metallic nodes, which produces numerous structural motifs. Furthermore, the intrinsic properties of MOFs including structural rigidity and permanent porosity can provide uniform active sites and open channels for chemo-, shape-, size-, and stereo-selective interactions.^{8–10} Owing to the aforementioned advantages, 2D MOFs have been widely applied in chemical sensing,^{11–13} catalysis,^{14,15} gas separation,¹⁶ and electronics^{7,17–19} with layered protonic conductive MOFs attracting most attention as an emerging class of clean energy-related materials.

Proton-conductive materials are of great interest because they can be candidates for electrolytes in sensors, batteries, and fuel cells.^{20,21} Owing to the designability of MOFs, several rules can be followed. First, guided by Pearson's hard/soft acid/base principle, the selection of metal node is important in constructing proton-conducting materials. High-valent metal ions are often selected to link with carboxylate ligands so that the resulting materials remain stable toward moisture under operating conditions.²² Second, ionic frameworks accompanied by the charge-balancing counterions are predicted to be more superior. For example, the anionic $[\text{In}(\text{COO})_4]^-$

Progress and Potential

Porous metal-organic frameworks (MOFs) combining both high proton and high electrical conductivity are poised to bring unprecedented opportunities to clean energy technologies such as new designs of fuel cells. However, so far, this unique class of materials has been elusive. Here, we present rational design of an MOF that displays exceptionally high proton conductivity by implementing proton-conveying functional groups onto the wall of its pores. Furthermore, this material is constructed by a redox-active ligand that enables efficient charge transfer between the MOF and the metal electrode in an electrical device. This leads to a high apparent electrical conductivity through a coupled ionic/pseudo-capacitive conduction mechanism. Thus, our work elaborates design principles for realizing efficient proton and electrical conduction in MOFs, extending their future applications to a variety of functional electronic, neuromorphic, and energy-conversion/storage devices.



node in the constructed In-MOFs are well known for their tendency to form a negatively charged framework with mobile charge-balancing species such as $\text{NH}_2(\text{CH}_3)_2^+$ (DMA), NH_4^+ , and H_3O^+ , and such features may enhance the proton conductivity.^{23,24} Third, the introduction of functional groups to adjust the pore micro-environments of MOFs is another effective approach to improve their proton conductivity.²⁵ Several specific base/acid groups, including imidazole,^{26,27} NH_3 ,²⁸ sulfonic,^{29,30} phosphonic,³¹ and carboxylic groups,^{32,33} have been incorporated into MOFs for enhanced proton conductivity, as they can tune the hydrophilicity of the pore surface, confer protons, and form hydrogen bonds as the proton migration pathway.³⁴ It is also worth noting that although three-dimensional (3D) proton-conductive MOFs have been developed, 2D proton-conductive MOFs are rarely reported. Most importantly, the proton (ion) and electron conduction have not yet been coupled in a single MOF structure, despite the possibility and unique advances demonstrated in conjugated polymers.^{35–39} Therefore, it is important to expand the design and synthetic strategies for the construction of novel 2D MOFs with enhanced conductivities and a mixed conduction mechanism.

Based on these design principles, we prepared two 2D proton-conductive MOFs, $[(\text{CH}_3)_2\text{NH}_2][\text{In}(m\text{-TTFTB})]$ (**1**) and $[(\text{CH}_3)_2\text{NH}_2][\text{In}(\text{TFFOC})]$ (**2**) (Figure 1), assembled from In^{3+} and redox-active tetrathiafulvalene (TTF)-based linkers ($m\text{-H}_4\text{TTFTB}$, H_8TFFOC , see Figures 1B and 1F). The highest proton conductivity of **2** reaches $1.69 \times 10^{-2} \text{ S cm}^{-1}$ at 343 K and 98% relative humidity (RH), which results from an efficient proton-conduction pathway consisting of dimethylammonium cation, water molecules, and uncoordinated carboxylic acid groups in its structure. Although **2** is a pure proton conductor without any efficient electrical conduction pathway, it exhibits a high direct current (DC) electrical conductivity in a humid environment ($4.05 \times 10^{-3} \text{ S cm}^{-1}$ at 303 K and 90% RH) when it is integrated into a resistor device with gold electrodes. We attribute the overall electrical conduction in this device to the proton conduction in **2** and the protonic/pseudo-capacitance coupling at the MOF-gold interface, the latter of which likely originates from the redox-switchable behavior of TTF-based ligands. This unprecedented charge-transport mechanism offers a new principle for utilizing the ionic conductivity from MOFs to construct functional electronic devices.

RESULTS AND DISCUSSION

Crystal Structures of 2D MOFs

Crystals of **1** were produced by reacting $\text{In}(\text{NO}_3)_3 \cdot 4\text{H}_2\text{O}$ with $m\text{-H}_4\text{TTFTB}$ via solvothermal synthesis. Single-crystal X-ray diffraction (XRD) analysis of **1** (Tables S1 and S2) revealed a layered structure with negatively charged 2D sheets and $(\text{CH}_3)_2\text{NH}_2^+$ counterions. The $m\text{-TTFTB}^{4-}$ coordinates to four $\text{In}(\text{III})$ with its four carboxylates in chelating bidentate modes and the eight-coordinated $\text{In}(\text{III})$ ion acts as the center of a distorted square antiprism (Figure S1). The four-connected $m\text{-TTFTB}^{4-}$ are linked by the $[\text{In}(\text{COO})_4]$ node with the one-dimensional hexagonal channel (Figures 1C and S2). The extensive interconnection of $m\text{-TTFTB}^{4-}$ ligands and $\text{In}(\text{COO})_4$ nodes results in a 2D sheet with thickness of about 10.1 Å (Figures 1A and S3). As shown in Figure 1D, the adjacent layers are linked by guest molecules with hydrogen bonds to form a 3D framework with pores. In this structure, there is no unbound carboxylic acid group; thus, proton conduction in **1** is likely conveyed by $(\text{CH}_3)_2\text{NH}_2^+$ cations and water molecules in the pores.

Based on the structure of **1**, we rationally designed another 2D MOF with free carboxylic acid groups that likely improve proton conductivity. Noticing that the H

¹State Key Laboratory of Coordination Chemistry, School of Chemistry and Chemical Engineering, Collaborative Innovation Center of Advanced Microstructures, Nanjing University, Nanjing 210023, China

²Key Laboratory of Mesoscopic Chemistry, School of Chemistry and Chemical Engineering, Nanjing University, Nanjing 210023, China

³Jiangsu Key Laboratory of Biofunctional Materials, School of Chemistry and Materials Science, Nanjing Normal University, Nanjing 210023, China

⁴Department of Chemistry, Northwestern University, 2145 Sheridan Road, Evanston, IL 60208, USA

⁵These authors contributed equally

⁶Lead Contact

*Correspondence: yqlan@njun.edu.cn (Y.-Q.L.), mding@nju.edu.cn (M.D.), zuoji@nju.edu.cn (J.-L.Z.)

<https://doi.org/10.1016/j.matt.2019.12.018>

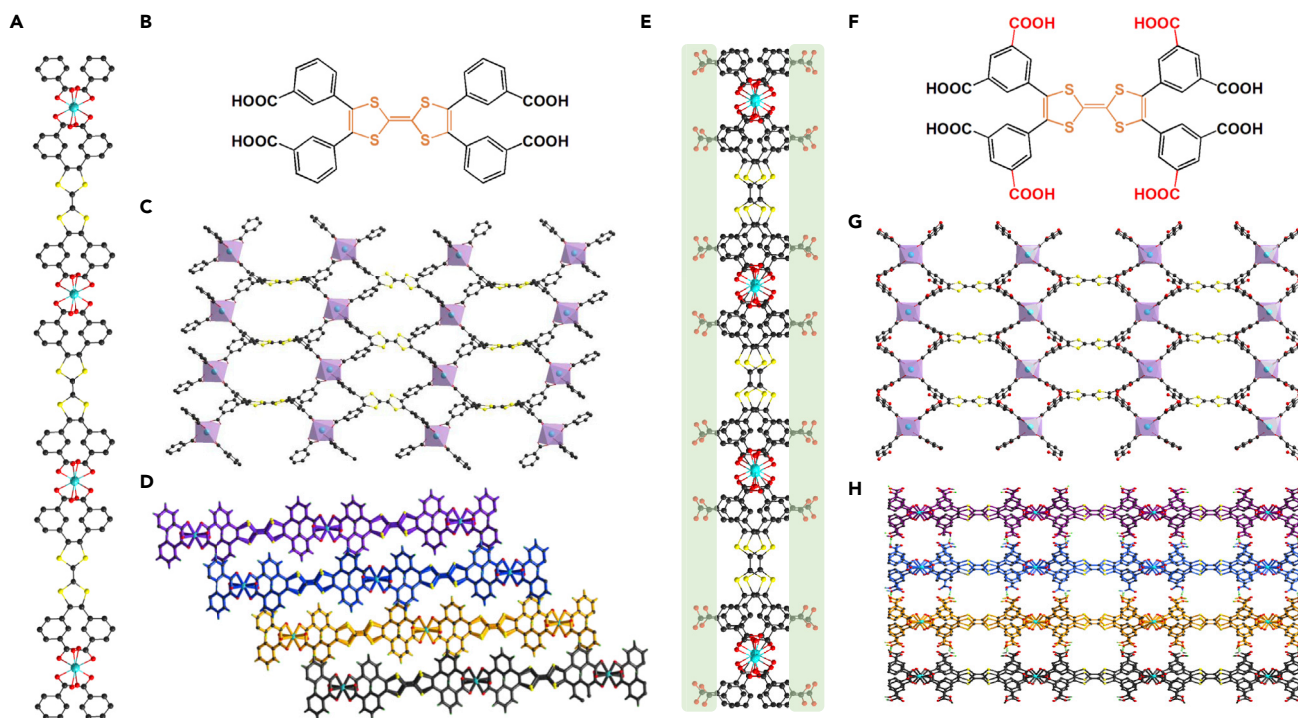


Figure 1. Structures of 2D MOFs 1 and 2

(A and E) The one-dimensional chain of 1 (A) and 2 (E).

(B and F) Structures of ligands *m*-H₄TTFTB (B) and H₈TTFOC (F).

(C and G) The carboxylate groups in black bind to In³⁺ ions, whereas the red ones are unbound carboxylic acid groups; the 2D network of 1 (C) and 2 (G).

(D and H) 3D stacking mode of 1 (D) and 2 (H). Color scheme: red, O; dark gray, C; yellow, S; green, H; cyan, In.

atom at the 5 position of each benzene ring of the *m*-TTFTB⁴⁻ ligand points to the adjacent layer in 1, we anticipated that replacing these H atoms by carboxylic acid groups may maintain the 2D sheet structure while introducing free carboxylic acid groups between sheets. Accordingly, we designed and synthesized the ligand H₈TTFOC, reacted it with In(NO₃)₃·4H₂O in similar conditions to the synthesis of 1, and obtained a 2D MOF, 2 (Tables S1 and S3). As expected, 2 is also a layered material with negatively charged 2D sheets and (CH₃)₂NH₂⁺ counterions. The structure of the 2D sheet in 2 is analogous to that in 1. The inner four carboxylate groups of the TTFOC⁴⁻ ligand coordinate to In³⁺, while the outer four carboxylic acid groups are unbound (Figures S4 and S5). These free carboxylic acid groups form O–H···O hydrogen bonds with those from the adjacent sheets, forming a proton-rich 3D porous structure (Figures 1H and S6). These free carboxylic acid groups cooperating with (CH₃)₂NH₂⁺ cations and water molecules likely form efficient proton-conduction pathways. The PLATON⁴⁰ calculations based on 2 give a total solvent-accessible volume of 5,747.8 Å³ per unit cell, equivalent to 64.1% of the total crystal volume. It is worth noting that the solvent-accessible volume of 2 is nearly twice that of 1 (32.1%, 1,631.2 Å³ per unit cell), owing to the stable hydrogen bonding between these carboxylates.

Probing the Redox Activity of 2D MOFs

The phase purities of 1 and 2 were confirmed by matching powder XRD (PXRD) patterns with their simulated patterns from single-crystal XRD (Figures S7 and S8). Interestingly, the redox activity of the ligands (*m*-H₄TTFTB, H₈TTFOC) (Figure S9) could

be a good inheritance for the assembled 2D MOFs **1** and **2** (Figure S10). To investigate the redox activity of ligands, we conducted cyclic voltammetry (CV) of *m*-H₄TTFTB and H₈TTFOC in 0.1 M LiBF₄ in *N,N*-dimethylformamide (DMF). Upon scanning anodically, two reversible one-electron processes at 0.18 and 0.50 V and 0.17 and 0.42 V, respectively (versus Fc/Fc⁺) were observed (Figure S9). These processes are attributed to the TTF/TTF^{•+} and TTF^{•+}/TTF²⁺ redox couples, respectively. The solid-state DC CV studies on **1** and **2** were conducted in 0.1 M LiBF₄ in CH₃CN (Figure S10). Upon scanning anodically, two quasi-reversible one-electron processes at 0.17 and 0.50 V and 0.27 and 0.59 V, respectively (versus Fc/Fc⁺) were observed. These processes are attributed to the TTF/TTF^{•+} and TTF^{•+}/TTF²⁺ redox couples, respectively.^{24,41,42}

Proton-Conduction Study of 2D MOFs

Many frameworks based on the TTF linkers have been reported,^{24,43–45} wherein Mg₂H₆(H₃O)(TTFTB)₃ (MIT-25) was found to be a proton conductor.⁴⁶ In our work, both **1** and **2** exhibit preferable structural stability to moisture according to the results of PXRD characterization in a humid environment (Figures S11 and S12). Proton conductivities of pressed pellets of **1** and **2** were determined by electrochemical impedance spectroscopy (Figures 2A and 2B). As shown in Figure 2A, the semicircle at the high-frequency region originates from the bulk and grain boundary resistances, yet the tail at the low-frequency region corresponds to the mobile ions clogged by the electrode-electrolyte interface.⁴⁷ Additionally, there are two clear semicircles in Figure 2B, which correspond to the bulk and grain boundary resistances together with electrode contribution.⁴⁸ The measurements were conducted at 303 K with various humidity to elucidate the correlation between proton conductivity and RH, the results of which can be found in Figures S13 and S14. At 40% RH, the proton conductivity of **1** is a negligible value of $5.57 \times 10^{-10} \text{ S cm}^{-1}$, whereas the proton conductivity of **2** is $2.58 \times 10^{-6} \text{ S cm}^{-1}$, which is nearly four orders of magnitude higher than that of **1**. With increasing RH, the proton conductivity of **1** increases to $6.66 \times 10^{-4} \text{ S cm}^{-1}$ at 98% RH, with the proton source presumably being the adsorbed H₂O molecules and (CH₃)₂NH₂⁺ ions in the pores (Figure 2F). At the same condition of 98% RH, the proton conductivity of **2** reaches $1.30 \times 10^{-2} \text{ S cm}^{-1}$ (more than 20-fold that of **1**). The positive correlation between proton conductivity of **1** and **2** and RH indicates that the proton conduction in these materials is mainly water mediated, which is typically improved by orders of magnitude with increasing RH even in a narrow range of high RHs. We attribute the high proton conductivity of **2** to its free carboxylic acid groups that function as both proton sources and conductive paths. In the structure of **2**, three components including carboxylic acid groups, dimethylamine cations, and water molecules form a proton-conduction pathway (indicated by the green ribbon in Figure 2G) and synergistically endow **2** with high proton conductivity.

To understand the proton-conduction mechanism in **1** and **2**, we performed variable-temperature proton conductivity measurements at 98% RH (Figures S15 and S16). Upon increasing temperature in the range of 303–343 K, the highest proton conductivities (at 343 K and 98% RH) for **1** and **2** were determined to be 7.39×10^{-3} and $1.69 \times 10^{-2} \text{ S cm}^{-1}$, respectively, and their equivalent circuits are shown in Figures S17 and S18. The relationship between proton conductivity and temperature was fitted with the Einstein-Nernst equation, which reveals the activation energies of these materials, providing insights into their proton-conduction mechanism (Figures 2C and 2D). At 98% RH, the activation energy values (E_a) for **1** and **2** are 0.59 and 0.09 eV, respectively. These distinct activation energies suggest different proton-conducting mechanisms in the two 2D MOFs: the proton conduction in **1** is

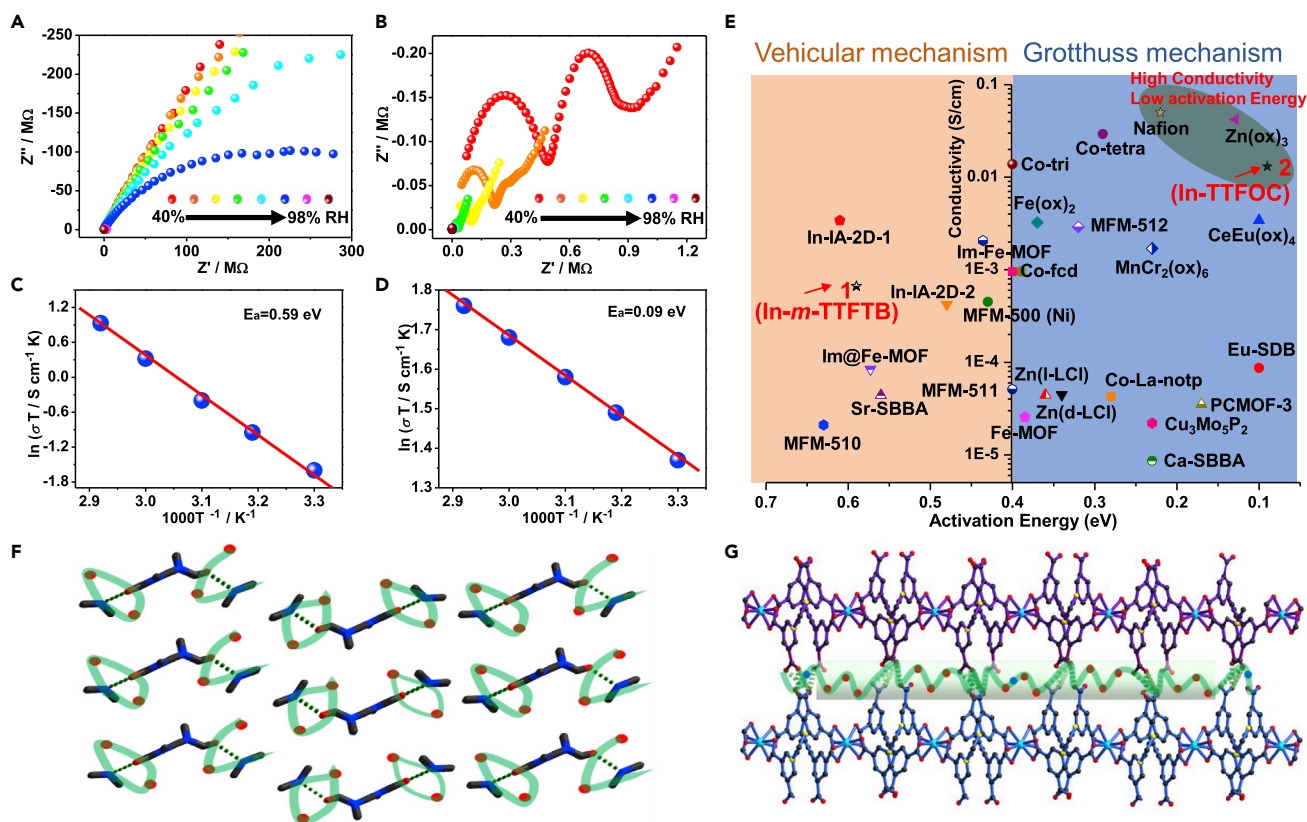


Figure 2. Proton Conduction of 2D MOFs 1 and 2

(A and B) Nyquist plots of 1 (A) and 2 (B) at 303 K and different RHs (40%, 50%, 60%, 70%, 80%, 90%, 95%–98% RH).

(C and D) Conductivity at 98% RH as a function of temperature in the range of 303–343 K of 1 (C) and 2 (D), where the solid lines (red) represent fitting curves based on the Einstein-Nernst equation that reveals the values of activation energy (E_a).

(E) Scatter diagram of 1 (In-*m*-TTFTB), 2 (In-TTFOC), commercial Nafion, and some other reported values of proton conductivity and activation energy at around 303 K and 98% RH.

(F and G) The hypothetical hydrogen-bonding nets in 1 (F) and 2 (G) in which the proton comes through, where the green lines represent hydrogen bonds, the red dots H_2O or H_3O^+ , and the blue dots the $\text{NH}_2(\text{CH}_3)_2^+$, all of which together with the uncoordinated carboxylic acid ($-\text{COOH}$) groups form a proton-conduction pathway, indicated by the green ribbon in (G).

consistent with the vehicular mechanism⁴⁹ ($E_a > 0.4$ eV), whereas it follows the Grotthuss mechanism⁵⁰ ($E_a < 0.4$ eV) in 2. Notably, compared with the widely used commercial proton conductor, Nafion, as well as several of the highest-performing MOFs under similar conditions (Table S4 and Figure 2E), 2 exhibits comparative proton conductivity and significantly lower activation energy, which demonstrates more efficient proton conduction in this MOF.

Combining crystal structures and proton-conduction activation energies of 1 and 2, further analysis can be performed to gain more insight into the proton-conduction pathways and mechanisms. For 1, the small and non-hydrophilic pores may prevent the formation of effective hydrogen-bonding networks (i.e., proton-conduction pathways). Moreover, the structure of 1 lacks the sites for proton transfer owing to the absence of proton sources and hydrogen-bonding nets. Thus, the proton conduction in 1 is likely dominated by the dynamic motion or rotation of guests in the channels, resulting in a high activation energy and vehicular mechanism. In contrast, for 2, the adsorbed water molecules, coordinated water molecules, the dimethylammonium cations, and, importantly, the assistance of the uncoordinated carboxylic

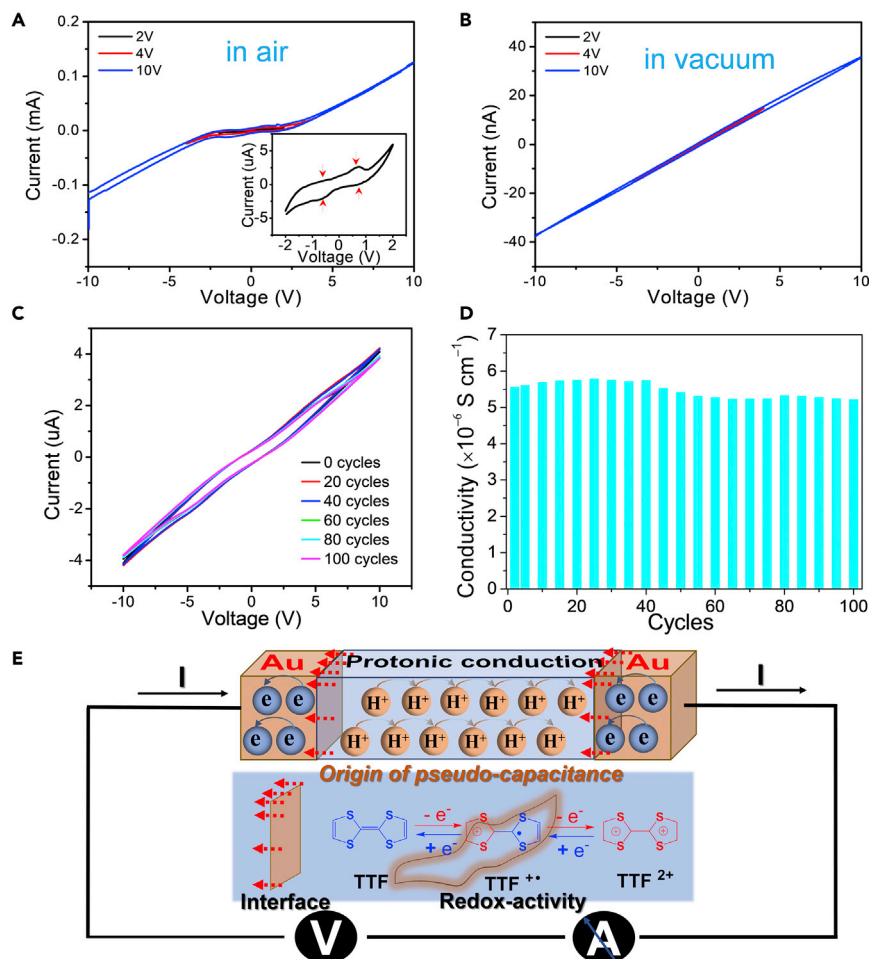


Figure 3. Apparent Electrical Conduction of 1 and 2

(A and B) Electron conductivity of 2 in air (A) and in vacuum (B). Inset: non-linear I - V curve with two couples of peaks in the range -2 V to 2 V.

(C) Current-voltage characteristics of 2 under 100 cycles in the condition of 303 K and 50% RH.

(D) Electron conductivity-time plot of 2 within 100 cycles at 303 K and 50% RH.

(E) Schemed circuit diagram and the redox reaction in the interface of 2 and Au electrode.

groups construct a rich hydrogen-bonding network in the channels of the framework for proton hopping (Grotthuss mechanism), leading to a lower E_a and higher proton conductivity.^{45,51,52}

Interfacial Pseudo-Capacitance for Overall Electrical Conduction

It is practically critical to integrate the organic conducting materials into a functional device.^{35–39} In this study, the 2D MOFs 1 and 2 were investigated for overall DC electrical conductivity as they were placed in contact with metal electrodes (see [Experimental Procedures](#); [Figures S19, S20, 2A, and 2B](#)). The typical current-voltage (I - V) curves of 2 are shown in [Figure 3](#). In ambient conditions (303 K and 90% RH), interestingly, 2 exhibits a non-linear I - V behavior ([Figure 3A](#)). Above a voltage barrier of ~ 2 V, the current density reaches the magnitude of 0.8 mA cm^{-2} , corresponding to a conductivity of $4.05 \times 10^{-3} \text{ S cm}^{-1}$, similar to the proton conductivity of 2 ($3.39 \times 10^{-3} \text{ S cm}^{-1}$ under 303 K and 90% RH), indicating a full integration of ionic conduction into the overall electrical circuit. Such high electrical conductivity is in significant

distinction to our previously reported 3D MOF, In-TTFTB.²⁴ To the best of our knowledge, this is the first demonstration of overall electrical conductivity from ion-conductive MOFs with metal contacts, and the apparent conductivity is comparable with conductive MOFs with intrinsic electron conduction.^{4,46,48} For pure ionically conductive materials, the lack of interfacial charge transfer pathway usually blocks the conduction pathway, and therefore only lead to an overall capacitive charging behavior. To probe the conducting mechanism of **2**, we further conducted the measurements in a vacuum. The *I-V* curves showed a linear behavior in this case, which translates to a conductivity of $1.69 \times 10^{-8} \text{ S cm}^{-1}$, much lower than that in ambient conditions (Figure 3B). This result highly resembles the aforementioned established trend in ion conductivity with different humidity (Figure 2B), indicating that (1) the high proton conductivity (in ambient conditions) is key to the ambient electrical conductivity in **2**; and (2) no (or neglectable) electron conduction (in a vacuum), which is necessary to comply with a “mixed ionic/electronic conduction” mechanism,^{35–39} is present in **2**.

Due to the lack of an electron/proton conduction pathway at the MOF-metal interface, an electrochemical (faradic) process is presumably responsible for the interfacial current density necessary for the overall electrical conductivity. The solid CV results showed that the redox activity of the ligands could be a good inheritance for the assembled 2D MOFs **1** and **2** (Figures S9 and S10). Therefore, we propose that the unique redox-switchable ligand TTF can serve as the electrochemically active component while the corresponding switches between its oxidation states provide a faradic current (as also proved by solid-state CV, Figure S10) that is high enough to match up to the ionic current density in the MOF channel. Such an interfacial faradic process can also be described as ligand-enabled pseudo-capacitance.

Cycling tests, stability tests, and other control experiments were further conducted to exclude the possibility of MOF degradation, which may also contribute to the interfacial charge transfer and cause the special electron-conducting phenomenon. First, the electrical conductivity of *m*-H₄TTFTB and H₈TTFOC linkers were measured in air, in a vacuum, and at various applied voltages up to 10 V (Figures S21–S24). Both linkers displayed consistent conductivity values in these conditions (2.74×10^{-8} , $1.37 \times 10^{-8} \text{ S cm}^{-1}$ for *m*-H₄TTFTB; 3.44×10^{-6} , $4.26 \times 10^{-6} \text{ S cm}^{-1}$ for H₈TTFOC in air and in vacuum, respectively), indicating electrical stability of these redox-active centers against air, vacuum, and applied bias. Second, we cycled a pressed pellet of **2** between -10 V and 10 V at 303 K and 50% RH 100 times, and extracted electrical conductivity from the *I-V* curve of each cycle (Figure 3C). Upon cycling, the electrical conductivity almost remained constant with only a 4.2% decrease after 100 cycles (Figure 3D). Third, we held the applied voltage at 10 V for a pressed pellet of **2** for 2.5 h. The current only slightly decreased, by 6.3%, within 2.5 h (Figures 3C and S25). It is worth noting that in this condition (303 K and 50% RH), **2** exhibits an overall conductivity of $5.56 \times 10^{-6} \text{ S cm}^{-1}$ that is almost identical to its proton conductivity ($5.95 \times 10^{-6} \text{ S cm}^{-1}$ under 303 K and 50% RH), indicating a full integration of ionic conduction into the overall electrical circuit (Figure 3C). Moreover, the electron conductivity observed in multiple devices is highly consistent with the average value being $6.66 \times 10^{-6} \text{ S cm}^{-1}$ and the standard deviation being $1.41 \times 10^{-6} \text{ S cm}^{-1}$ (Figure S26). The PXRD patterns of the sample of **2** that has been subjected to the aforementioned experiments shows that its crystallinity is comparable with that of the pristine sample, verifying the structural stability of **2** (Figure S27). In summary, these results provide solid experimental evidence to exclude the possibility of interfacial decomposition in the electrical measurement and confirm the ionic-capacitive conduction mechanism.

The schematic illustration of this mechanism, the “coupled ionic/pseudo-capacitive conduction” model, is shown in Figure 3E. Under the DC electric field, the protons in **2** move within the MOF channel while the redox reaction of TTF affords the simultaneous charge transfer at the interface. This model is further supported by the observation in the low-current region (–2 to 2 V) in Figure 3A (inset), where two redox-mediated conductive regions are clearly shown in the *I*-*V* curve. This result indicates the redox-switching origin of the electrical barrier, and matches the “coupled ionic pseudo-capacitance” model. In addition, the same *I*-*V* measurements for **1** yielded a different result for the same applied voltage: the *I*-*V* curves appear linear and conductivities are low in both ambient ($8.72 \times 10^{-10} \text{ S cm}^{-1}$) and vacuum ($9.65 \times 10^{-10} \text{ S cm}^{-1}$) conditions (Figures S19 and S20). This result further confirms that ultrahigh current density requires high ionic conductivity, which only exists in MOF **2**, whereas the low proton conductivity of compound **1** ($4.66 \times 10^{-9} \text{ S cm}^{-1}$ at 303 K and 90% RH) limits the overall electrical conduction, despite its similar pseudo-capacitance at the interface (Figure S10B).

Conclusions

In conclusion, we designed and successfully synthesized an interesting 2D superprotonic conductive MOF containing redox TTF-octacarboxylates and distorted square antiprism $\text{In}(\text{COO})_4$ node. The proton conductivity of **2** with H_8TTFOC ($1.30 \times 10^{-2} \text{ S cm}^{-1}$ at 303 K and 98% RH) is higher than that of **1** with *m*- H_4TTFTB ($6.66 \times 10^{-4} \text{ S cm}^{-1}$ at 303 K and 98% RH), and these two compounds showed different proton-transfer mechanisms. Overall, the method of space-install of additional carboxylic groups on 2D MOFs could be an effective way to improve the proton conductivity. The redox-active 2D MOF, **2**, with excellent proton conductivity and interfacial pseudo-capacitance, enabled by its unique out-of-plane protonic channels and redox-switchable ligands, creates an unprecedented “coupled ionic/pseudo-capacitive conduction” that results in an ultrahigh electrical conduction from an ionic conductive MOF material. This new mechanism will enrich the design and synthetic principles of the ion-conductive 2D MOFs, extending their future applications to a variety of functional electronic, neuromorphic, and energy-conversion/storage devices.

EXPERIMENTAL PROCEDURES

Synthesis of *m*- $\text{Et}_4\text{-TTFTB}$

m- H_4TTFTB was prepared by adopting the procedure reported by our group (Scheme S1).²⁴ $\text{Pd}(\text{OAc})_2$ (410 mg, 1.83 mmol), $\text{P}(\text{t-Bu})_3 \cdot \text{HBF}_4$ (1.60 g, 5.51 mmol), and Cs_2CO_3 (12 g, 36.83 mmol) were placed in a 250-mL reaction flask under nitrogen. The degassed THF (100 mL) was added and the mixture was stirred for 30 min with heating at 60°C. Tetrathiafulvalene (1.5 g, 7.34 mmol) and ethyl *m*-bromobenzoate (9.47 g, 41.34 mmol) was added. The mixture was heated at reflux for 72 h. The product was concentrated *in vacuo* to solid. The organic compounds were extracted with dichloromethane (DCM) through filtration and concentrated *in vacuo*. Chromatographic purification on silica gel by using petroleum ether/DCM (1:3) as an eluent afforded *m*- $\text{Et}_4\text{-TTFTB}$ (2.2 g, 2.76 mmol, 37.6%) as an orange solid. $^1\text{H NMR}$ (400 MHz, CDCl_3) δ 7.96 (m, 8H), 7.36 (m, 8H), 4.33 (q, 8H), 1.35 (t, 12H); electrospray ionization mass spectrometry (ESI-MS) (acetonitrile) *m/z* calcd for $\text{C}_{46}\text{H}_{36}\text{O}_8\text{S}_4$ [M^+] 796.13, found 796.17; element analysis calcd: C, 63.29; H, 4.55%; found: C, 62.98; H, 4.70%. IR (KBr, cm^{-1}): 2,979 m, 2,904 w, 2,360 w, 1,718 vs, 1,600 w, 1,581 w, 1,474 w, 1,431 w, 1,392 w, 1,366 s, 1,297 vs, 1,232 vs, 1,185 m, 1,104 s, 1,083 s, 1,026 m, 919 w, 865 w, 821 w, 782 w, 748 s, 692 s, 644 w, 626 w, 440 w.

Synthesis of *m*-H₄TTFTB

m-Et₄-TTFTB (4.10 g, 5.14 mmol) and THF (150 mL)/MeOH (150 mL) were placed in a 500-mL reaction flask under air. A solution of KOH (4.0 g, 71.28 mmol) dissolved in 30 mL water was added and the mixture was stirred overnight with heating at 90°C. The product was concentrated *in vacuo* to red oil or solid. Water (60 mL) was added to dissolve the red solid. HCl was added to adjust the solution to pH 2. The red solid was obtained by centrifugation and washed three times with water. After vacuum drying, *m*-H₄TTFTB (3.22 g, 4.70 mmol, 81%) was afforded as a red solid. ¹H NMR (400 MHz, d₆-DMSO) δ 13.15 (brs, 4H), 7.89 (m, 4H), 7.79 (s, 4H), 7.45 (m, 8H); ESI-MS (methanol) *m/z* calcd for C₃₄H₂₀O₈S₄ [M-H]⁻ 683.00, found 683.08; element analysis calcd: C, 59.63; H, 2.94%; found: C, 59.38; H, 2.76%. IR (KBr, cm⁻¹): 3,026 w, 2,531 w, 1,696 vs, 1,600 m, 1,581 m, 1,482 m, 1,441 m, 1,408 m, 1,297 s, 1,196 m, 1,083 m, 919 m, 816 m, 747 s, 685 s, 555 m, 437 w.

Synthesis of Me₈-TTFOC

H₈TTFOC was prepared by adopting the procedure reported by our group (Scheme S1).²⁴ Pd(OAc)₂ (274 mg, 1.22 mmol), P(*t*-Bu)₃•HBF₄ (1.06 g, 3.65 mmol), and Cs₂CO₃ (8 g, 24.55 mmol) were placed in a 250-mL reaction flask under nitrogen. Degassed 1,4-dioxane (100 mL) was added and the mixture was stirred for 30 min with heating at 60°C. Tetrathiafulvalene (1.0 g, 4.89 mmol) and dimethyl 5-bromoisophthalate (6.66 g, 24.39 mmol) was added. The mixture was heated at reflux for 72 h. The product was concentrated *in vacuo* to solid. The organic compounds were extracted with dichloromethane through filtration and concentrated *in vacuo*. Chromatographic purification on silica gel by using DCM or DCM/methanol (100:1) as an eluent afforded Me₈-TTFOC (1.2 g, 1.23 mmol, 25%) as an orange solid. ¹H NMR (400 MHz, CDCl₃) δ 8.58 (s, 4H), 8.07 (m, 8H), 3.89 (s, 24H); ESI-MS (acetonitrile) *m/z* calcd for C₄₆H₃₆O₁₆S₄ [M]⁺ 972.09, found 972.08; element analysis calcd: C, 56.78; H, 3.73%; found: C, 56.24; H, 3.51%. IR (KBr, cm⁻¹): 3,533 w, 2,955 w, 2,361 w, 1,726 vs, 1,598 w, 1,563 w, 1,439 s, 1,336 s, 1,251 vs, 1,200 w, 1,135 w, 1,046 w, 1,000 m, 918 w, 882 w, 782 w, 752 s, 721 s, 687 w, 649 w, 447 m.

Synthesis of H₈TTFOC

Me₈-TTFOC (0.63 g, 0.65 mmol) and EtOH (20 mL) were placed in a 100-mL reaction flask under air. A solution of KOH (0.50 g, 8.91 mmol) dissolved in 2 mL of water was added and the mixture was stirred overnight with heating at 90°C. The product was concentrated *in vacuo* to red oil or solid. Water (20 mL) was added to dissolve the red solid. HCl was added to adjust the solution to pH 2. The dark-red solid was obtained by centrifugation and washed three times with water. After vacuum drying, H₈TTFOC (0.50 g, 0.58 mmol, 89%) was afforded as a black solid. ¹H NMR (400 MHz, d₆-DMSO) δ 13.49 (brs, 8H), 8.37 (t, 4H), 7.98 (m, 8H); ESI-MS (methanol) *m/z* calcd for C₃₈H₂₀H₁₆S₄ [M-H]⁻ 858.96, found 859.08; element analysis calcd: C, 53.02; H, 2.34%; found: C, 52.76; H, 2.10%. IR (KBr, cm⁻¹): 3,567 w, 2,361 w, 1,700 s, 1,653 s, 1,559 s, 1,436 m, 1,360 w, 1,230 s, 1,040 w, 908 w, 758 s, 675 s, 492 s, 452 m.

Synthesis of [(CH₃)₂NH₂][In(*m*-TTFTB)]•DMF•5H₂O (Compound 1)

To a solution of *m*-H₄TTFTB (0.010 g, 0.014 mmol) and 4,4'-bipy (0.010 g, 0.064 mmol) in 2 mL of DMF was added a solution of In(NO₃)₃•4H₂O (0.010 g, 0.027 mmol) in 0.3 mL of H₂O, followed by 0.15 mL of CH₃COOH. The mixture was heated to 120°C for 24 h and allowed to cool to room temperature. Red block crystals (0.005 g) were obtained by filtration and washed three times with DMF and CH₃COCH₃. Yield 29% (based on *m*-H₄TTFTB). Calcd for C₃₉H₇₁N₂O₂₉S₄In (Mr = 1,275.06): C, 36.74; H, 5.61; N, 2.20%. Found: C, 37.21; H, 5.32; N, 2.40%. IR (KBr, cm⁻¹): 3,059 br, 2,928 br, 2,360 w, 1,663 vs, 1,617 s, 1,593 s, 1,565 s, 1,439 vs,

1,387 vs, 1,205 w, 1,168 w, 1,090 s, 1,019 m, 998 m, 921 m, 882 m, 849 m, 832 m, 815 m, 775 s, 764 vs, 703 vs, 668 m, 624 m, 563 w, 544 w, 513 w, 447 s.

Synthesis of $[(\text{CH}_3)_2\text{NH}_2][\text{In}(\text{H}_4\text{TTFOC})] \cdot 5\text{DMF} \cdot 13\text{H}_2\text{O}$ (Compound 2)

To a solution of H_8TTFOC (0.010 g, 0.012 mmol) in 2 mL of DMF was added a solution of $\text{In}(\text{NO}_3)_3 \cdot 4\text{H}_2\text{O}$ (0.010 g, 0.027 mmol) in 0.5 mL of H_2O , followed by 0.050 mL of H_2SO_4 . The mixture was heated to 120°C for 72 h and allowed to cool to room temperature at a rate of 5°C h^{-1} . Red block crystals (0.006 g) were obtained by filtration and washed three times with DMF and CH_3COCH_3 . Yield 31% (based on H_8TTFOC). Calcd for $\text{C}_{45}\text{H}_{89}\text{N}_6\text{O}_{34}\text{S}_4\text{In}$ ($M_r = 1,621.12$): C, 36.00; H, 5.98; N, 5.60%. Found: C, 35.89; H, 5.90; N, 5.48%. IR (KBr, cm^{-1}): 3,420 w, 1,700 s, 1,617 s, 1,559 s, 1,433 m, 1,362 w, 1,236 m, 1,041 m, 1,016 m, 920 m, 873 w, 776 s, 682 s, 642 w, 515 w, 447 m.

DATA AND CODE AVAILABILITY

Experimental Procedures for the detailed measurements, additional single-crystal structures, PXRD, solid-state cyclic voltammograms, current-voltage characteristics, and crystallographic data of the structure (CIF) are provided in [Supplemental Information](#). The X-ray crystallographic coordinates for structures reported in this article have been deposited at the Cambridge Crystallographic Data Center (CCDC) under deposition number CCDC: 1908181 and 1908182 for compounds 1 and 2, respectively. These data can be obtained free of charge from the CCDC via www.ccdc.cam.ac.uk/data_request/cif. All relevant data supporting the findings of this study are available from the corresponding authors on request.

SUPPLEMENTAL INFORMATION

Supplemental Information can be found online at <https://doi.org/10.1016/j.matt.2019.12.018>.

ACKNOWLEDGMENTS

This work was supported by the National Basic Research Program of China (2018YFA0306004) and the National Natural Science Foundation of China (21631006 and 21875099). M.D. acknowledges support by the Fundamental Research Funds for the Central Universities in China (020514380136), and the Natural Science Foundation of Jiangsu Province (BK20180321). L.S. thanks the Postdoctoral Program in Environmental Chemistry Award from the Camille and Henry Dreyfus Foundation.

AUTHOR CONTRIBUTIONS

Conceptualization, M.D. and J.-L.Z.; Methodology, J.S., W.H., X.-M.L., and L.S.; Investigation, J.-L.Z., M.D., J.S., W.H., X.-M.L., and L.S.; Formal Analysis, J.S., W.H., X.-M.L., L.S., and H.-Y.W.; Funding Acquisition, J.-L.Z. and M.D.; Resources, J.-L.Z., M.D., and Y.-Q.L.; Writing – Original Draft, J.-L.Z., J.S., X.-M.L., L.S., and M.D.; Writing – Review & Editing, all authors; Supervision, J.-L.Z., M.D., and Y.-Q.L.

DECLARATION OF INTERESTS

The authors declare no competing interests.

Received: July 12, 2019

Revised: November 7, 2019

Accepted: December 12, 2019

Published: January 22, 2020

REFERENCES

- Huang, X., Zeng, Z., and Zhang, H. (2013). Metal dichalcogenide nanosheets: preparation, properties and applications. *Chem. Soc. Rev.* *42*, 1934–1946.
- Xu, M., Liang, T., Shi, M., and Chen, H. (2013). Graphene-like two-dimensional materials. *Chem. Rev.* *113*, 3766–3798.
- Zhang, H. (2018). Introduction: 2D materials chemistry. *Chem. Rev.* *118*, 6089–6090.
- Zhao, M., Lu, Q., Ma, Q., and Zhang, H. (2017). Two-dimensional metal-organic framework nanosheets. *Small Methods* *1*, 1600030.
- Ko, M., Mendecki, L., and Mirica, K.A. (2018). Conductive two-dimensional metal-organic frameworks as multifunctional materials. *Chem. Commun. (Camb.)* *54*, 7873–7891.
- Zhao, M., Huang, Y., Peng, Y., Huang, Z., Ma, Q., and Zhang, H. (2018). Two-dimensional metal-organic framework nanosheets: synthesis and applications. *Chem. Soc. Rev.* *47*, 6267–6295.
- Zhao, W., Peng, J., Wang, W., Liu, S., Zhao, Q., and Huang, W. (2018). Ultrathin two-dimensional metal-organic framework nanosheets for functional electronic devices. *Coord. Chem. Rev.* *377*, 44–63.
- Liao, P.Q., Huang, N.Y., Zhang, W.X., Zhang, J.P., and Chen, X.M. (2017). Controlling guest conformation for efficient purification of butadiene. *Science* *356*, 1193–1196.
- Lustig, W.P., Mukherjee, S., Rudd, N.D., Desai, A.V., Li, J., and Ghosh, S.K. (2017). Metal-organic frameworks: functional luminescent and photonic materials for sensing applications. *Chem. Soc. Rev.* *46*, 3242–3285.
- Das, S., Xu, S., Ben, T., and Qiu, S. (2018). Chiral recognition and separation by chirality-enriched metal-organic frameworks. *Angew. Chem. Int. Ed.* *57*, 8629–8633.
- Yao, M.-S., Lv, X.-J., Fu, Z.-H., Li, W.-H., Deng, W.-H., Wu, G.-D., and Xu, G. (2017). Layer-by-layer assembled conductive metal-organic framework nanofilms for room-temperature chemiresistive sensing. *Angew. Chem. Int. Ed.* *56*, 16510–16514.
- Luo, Y.H., Chen, C., He, C., Zhu, Y.Y., Hong, D.L., He, X.T., An, P.J., Wu, H.S., and Sun, B.W. (2018). Single-layered two-dimensional metal-organic framework nanosheets as an in situ visual test paper for solvents. *ACS Appl. Mater. Interfaces* *10*, 28860–28867.
- Zhao, M., Wang, Y., Ma, Q., Huang, Y., Zhang, X., Ping, J., Zhang, Z., Lu, Q., Yu, Y., Xu, H., et al. (2015). Ultrathin 2D metal-organic framework nanosheets. *Adv. Mater.* *27*, 7372–7378.
- Xiao, Y., Qi, Y., Wang, X., Wang, X., Zhang, F., and Li, C. (2018). Visible-light-responsive 2D cadmium-organic framework single crystals with dual functions of water reduction and oxidation. *Adv. Mater.* *30*, 1803401.
- He, T., Ni, B., Zhang, S., Gong, Y., Wang, H., Gu, L., Zhuang, J., Hu, W., and Wang, X. (2018). Ultrathin 2D zirconium metal-organic framework nanosheets: preparation and application in photocatalysis. *Small* *14*, e1703929.
- Peng, Y., Li, Y., Ban, Y., and Yang, W. (2017). Two-dimensional metal-organic framework nanosheets for membrane-based gas separation. *Angew. Chem. Int. Ed.* *56*, 9757–9761.
- Wu, G., Huang, J., Zang, Y., He, J., and Xu, G. (2016). Porous field-effect transistors based on a semiconductive metal-organic framework. *J. Am. Chem. Soc.* *139*, 1360–1363.
- Nagatomi, H., Yanai, N., Yamada, T., Shiraishi, K., and Kimizuka, N. (2018). Synthesis and electric properties of a two-dimensional metal-organic framework based on phthalocyanine. *Chem. Eur. J.* *24*, 1806–1810.
- Pedersen, K.S., Perlepe, P., Aubrey, M.L., Woodruff, D.N., Reyes-Lillo, S.E., Reinholdt, A., Voigt, L., Li, Z., Borup, K., Rouzies, M., et al. (2018). Formation of the layered conductive magnet $\text{CrCl}_2(\text{pyrazine})_2$ through redox-active coordination chemistry. *Nat. Chem.* *10*, 1056–1061.
- Ramaswamy, P., Wong, N.E., and Shimizu, G.K. (2014). MOFs as proton conductors—challenges and opportunities. *Chem. Soc. Rev.* *43*, 5913–5932.
- Bao, S.-S., Shimizu, G.K.H., and Zheng, L.-M. (2019). Proton conductive metal phosphonate frameworks. *Coord. Chem. Rev.* *378*, 577–594.
- Yuan, S., Feng, L., Wang, K., Pang, J., Bosch, M., Lollar, C., Sun, Y., Qin, J., Yang, X., Zhang, P., et al. (2018). Stable metal-organic frameworks: design, synthesis, and applications. *Adv. Mater.* *30*, e1704303.
- Zhao, X., Mao, C., Bu, X., and Feng, P. (2014). Direct observation of two types of proton conduction tunnels coexisting in a new porous indium-organic framework. *Chem. Mater.* *26*, 2492–2495.
- Su, J., Yuan, S., Wang, H.Y., Huang, L., Ge, J.Y., Joseph, E., Qin, J., Cagin, T., Zuo, J.L., and Zhou, H.C. (2017). Redox-switchable breathing behavior in tetrathiafulvalene-based metal-organic frameworks. *Nat. Commun.* *8*, 2008.
- Bazaga-Garcia, M., Colodrero, R.M., Papadaki, M., Garczarek, P., Zon, J., Olivera-Pastor, P., Losilla, E.R., Leon-Reina, L., Aranda, M.A., Choquesillo-Lazarte, D., et al. (2014). Guest molecule-responsive functional calcium phosphonate frameworks for tuned proton conductivity. *J. Am. Chem. Soc.* *136*, 5731–5739.
- Ye, Y., Guo, W., Wang, L., Li, Z., Song, Z., Chen, J., Zhang, Z., Xiang, S., and Chen, B. (2017). Straightforward loading of imidazole molecules into metal-organic framework for high proton conduction. *J. Am. Chem. Soc.* *139*, 15604–15607.
- Zhang, F.M., Dong, L.Z., Qin, J.S., Guan, W., Liu, J., Li, S.L., Lu, M., Lan, Y.Q., Su, Z.M., and Zhou, H.C. (2017). Effect of imidazole arrangements on proton-conductivity in metal-organic frameworks. *J. Am. Chem. Soc.* *139*, 6183–6189.
- Liu, R., Zhao, L., Yu, S., Liang, X., Li, Z., and Li, G. (2018). Enhancing proton conductivity of a 3D metal-organic framework by attaching guest NH_3 molecules. *Inorg. Chem.* *57*, 11560–11568.
- Li, X.-M., Dong, L.-Z., Li, S.-L., Xu, G., Liu, J., Zhang, F.-M., Lu, L.-S., and Lan, Y.-Q. (2017). Synergistic conductivity effect in a proton sources-coupled metal-organic framework. *ACS Energy Lett.* *2*, 2313–2318.
- Phang, W.J., Jo, H., Lee, W.R., Song, J.H., Yoo, K., Kim, B., and Hong, C.S. (2015). Superprotonic conductivity of a UiO-66 framework functionalized with sulfonic acid groups by facile postsynthetic oxidation. *Angew. Chem. Int. Ed.* *54*, 5142–5146.
- Ramaswamy, P., Wong, N.E., Gelfand, B.S., and Shimizu, G.K. (2015). A water stable magnesium MOF that conducts protons over $10(-2)$ S cm (-1) . *J. Am. Chem. Soc.* *137*, 7640–7643.
- Rought, P., Marsh, C., Pili, S., Silverwood, I.P., Sakai, V.G., Li, M., Brown, M.S., Argent, S.P., Vitorica-Yrezabal, I., Whitehead, G., et al. (2019). Modulating proton diffusion and conductivity in metal-organic frameworks by incorporation of accessible free carboxylic acid groups. *Chem. Sci.* *10*, 1492–1499.
- Sadakiyo, M., Yamada, T., and Kitagawa, H. (2009). Rational designs for highly proton-conductive metal-organic frameworks. *J. Am. Chem. Soc.* *131*, 9906–9907.
- Horike, S., Umeyama, D., and Kitagawa, S. (2013). Ion conductivity and transport by porous coordination polymers and metal-organic frameworks. *Acc. Chem. Res.* *46*, 2376–2384.
- Berggren, M., Crispin, X., Fabiano, S., Jonsson, M.P., Simon, D.T., Stavrinidou, E., Tybrandt, K., and Zozoulenko, I. (2019). Ion electron-coupled functionality in materials and devices based on conjugated polymers. *Adv. Mater.* *31*, 1805813.
- Volkov, A.V., Wijeratne, K., Mitraka, E., Ail, U., Zhao, D., Tybrandt, K., Andreasen, J.W., Berggren, M., Crispin, X., and Zozoulenko, I.V. (2017). Understanding the capacitance of PEDOT: PSS. *Adv. Funct. Mater.* *27*, 1700329.
- Rivnay, J., Inal, S., Collins, B.A., Sessolo, M., Stavrinidou, E., Strakosas, X., Tassone, C., Delongchamp, D.M., and Malliaras, G.G. (2016). Structural control of mixed ionic and electronic transport in conducting polymers. *Nat. Commun.* *7*, 11287.
- Rivnay, J., Inal, S., Salleo, A., Owens, R.M., Berggren, M., and Malliaras, G.G. (2018). Organic electrochemical transistors. *Nat. Rev. Mater.* *3*, 17086.
- Berggren, M., and Malliaras, G.G. (2019). How conducting polymer electrodes operate. *Science* *364*, 233–234.
- Spek, A.L. (2003). Single-crystal structure validation with the program PLATON. *J. Appl. Crystallogr.* *36*, 7–13.
- Su, J., Hu, T.H., Murase, R., Wang, H.Y., D'Alessandro, D.M., Kurmoo, M., and Zuo, J.L. (2019). Redox activities of metal-organic frameworks incorporating rare-earth metal chains and tetrathiafulvalene linkers. *Inorg. Chem.* *58*, 3698–3706.
- Leong, C.F., Wang, C.-H., Ling, C.D., and D'Alessandro, D.M. (2018). A spectroscopic

and electrochemical investigation of a tetrathiafulvalene series of metal-organic frameworks. *Polyhedron* 154, 334–342.

43. Nguyen Tle, A., Demir-Cakan, R., Devic, T., Morcrette, M., Ahnfeldt, T., Auban-Senzier, P., Stock, N., Goncalves, A.M., Filinchuk, Y., Tarascon, J.M., et al. (2010). 3-D coordination polymers based on the tetrathiafulvalenetetracarboxylate (TTF-TC) derivative: synthesis, characterization, and oxidation issues. *Inorg. Chem.* 49, 7135–7143.
44. Leong, C.F., Chan, B., Faust, T.B., and D'Alessandro, D.M. (2014). Controlling charge separation in a novel donor-acceptor metal-organic framework via redox modulation. *Chem. Sci.* 5, 4724–4728.
45. Sun, L., Campbell, M.G., and Dinca, M. (2016). Electrically conductive porous metal-organic frameworks. *Angew. Chem. Int. Ed.* 55, 3566–3579.
46. Park, S.S., Rieth, A.J., Hendon, C.H., and Dinca, M. (2018). Selective vapor pressure dependent proton transport in a metal-organic framework with two distinct hydrophilic pores. *J. Am. Chem. Soc.* 140, 2016–2019.
47. Nagarkar, S.S., Unni, S.M., Sharma, A., Kurungot, S., and Ghosh, S.K. (2014). Two-in-one: inherent anhydrous and water-assisted high proton conduction in a 3D metal-organic framework. *Angew. Chem. Int. Ed.* 53, 2638–2642.
48. Ponomareva, V.G., Kovalenko, K.A., Chupakhin, A.P., Dybtsev, D.N., Shutova, E.S., and Fedin, V.P. (2012). Imparting high proton conductivity to a metal-organic framework material by controlled acid impregnation. *J. Am. Chem. Soc.* 134, 15640–15643.
49. Agmon, N. (1995). The Grotthuss mechanism. *Chem. Phys. Lett.* 244, 456–462.
50. Kreuer, K.-D., Rabenau, A., and Weppner, W. (1982). Vehicle mechanism, a new model for the interpretation of the conductivity of fast proton conductors. *Angew. Chem. Int. Ed.* 21, 208–209.
51. Narayan, T.C., Miyakai, T., Seki, S., and Dinca, M. (2012). High charge mobility in a tetrathiafulvalene-based microporous metal-organic framework. *J. Am. Chem. Soc.* 134, 12932–12935.
52. Park, S.S., Hontz, E.R., Sun, L., Hendon, C.H., Walsh, A., Van Voorhis, T., and Dinca, M. (2015). Cation-dependent intrinsic electrical conductivity in isostructural tetrathiafulvalene-based microporous metal-organic frameworks. *J. Am. Chem. Soc.* 137, 1774–1777.